ADVANCED FUNCTIONAL MATERIALS
www.afm-journal.de

High Power Conversion Efficiency of 13.61% for 1 cm^2 Flexible Polymer Solar Cells Based on Patternable and Mass-Producible Gravure-Printed Silver Nanowire Electrodes

Zhenguo Wang, Yunfei Han, Lingpeng Yan, Chao Gong, Jiachen Kang, Hao Zhang, Xue Sun, Lianping Zhang, Jian Lin, Qun Luo,* and Chang-Qi Ma**

With the aim of developing high-performance flexible polymer solar cells, the preparation of flexible transparent electrodes (FTEs) via a high-throughput gravure printing process is reported. By varying the blend ratio of the mixture solvent and the concentration of the silver nanowire (AgNW) inks, the surface tension, volatilization rate, and viscosity of the AgNW ink can be tuned to meet the requirements of gravure printing process. Following this method, uniformly printed AgNW films are prepared. Highly conductive FTEs with a sheet resistance of 10.8 Ω sq^{-1} and a high transparency of 95.4% (excluded substrate) are achieved, which are comparable to those of indium tin oxide electrode. In comparison with the spin-coating process, the gravure printing process exhibits advantages of the ease of large-area fabrication and improved uniformity, which are attributed to better ink droplet distribution over the substrate. 0.04 cm^2 polymer solar cells based on gravure-printed AgNW electrodes with PM6:Y6 as the photoactive layer show the highest power conversion efficiency (PCE) of 15.28% with an average PCE of 14.75 ± 0.35%. Owing to the good uniformity of the gravure-printed AgNW electrode, the highest PCE of 13.61% is achieved for 1 cm^2 polymer solar cells based on the gravure-printed FTEs.

1. Introduction

Polymer solar cells (PSCs) have received extensive attention owing to their numerous advantages, such as light weights, mechanical flexibility, and roll-to-roll solution fabrication compatibility.[1–5] In recent years, owing to the rapid developments in the synthesis of new organic semiconductors,[6–8] optimization of the active layer morphology,[9–11] and interface engineering,[12–14] the power conversion efficiency (PCE) of glass–indium tin oxide (ITO)-based single-junction PSCs has exceeded 18%.[15] However, the performance of flexible organic solar cells (OSCs) is still lagging,[16] particularly for large-area devices, owing to the lack of high-performance flexible transparent electrodes (FTEs). For use in flexible PSCs, high-performance FTEs are required, which exhibit low sheet resistance, high light transmittance, low surface roughness, excellent flexibility, large-area uniformity, and prepattern and mass production compatibility.[17–19]

Various conductive materials, such as graphene,[20,21] conductive polymers,[22,23] metal grids,[24–26] and metal nanowires,[2,27,28] have been reported for preparing high-performance FTEs. Among these, silver nanowire (AgNW) electrodes are recognized as the most promising owing to their high light transmittance, low sheet resistance, good processability, and excellent flexibility.[17,29] Both bottom[28–31] and top[32–34] electrodes using AgNW networks have been reported in polymer and perovskite solar cells. However, in terms of the FTE for PSCs, only a few studies have been conducted,[2,17,35–37] and these AgNW films were prepared by spin coating[2,36,37] or slot-die coating.[35] Note that spin coating cannot be directly transferred to the mass production line, and neither spin coating nor slot-die coating are prepatternable. Therefore, a new method that includes prepatterned electrode structures and is compatible with large-scale production is necessary for flexible polymer solar cell fabrication.

Gravure printing is efficient and can directly print the desired structure using a prepatterned gravure roller, in which inks in the patterned area are transferred to the substrate under pressure. It is the fastest printing method with a printing speed of up to 450 m min^{-1}, ensuring extremely high throughput in real applications. Most importantly, because the micrometer-scale cavities of the gravure roller are typically homogeneously distributed and impart high uniformity to the printed film,

Z. G. Wang, Y. F. Han, Dr. J. Lin, Dr. Q. Luo, Prof. C.-Q. Ma
School of Nano-Tech and Nano-Bionics
University of Science and Technology of China
Hefei 230026, P. R. China
E-mail: jlin2010@sinano.ac.cn; qluo2011@sinano.ac.cn; cqma2011@sinano.ac.cn

Z. G. Wang, Y. F. Han, Dr. L. P. Yan, C. Gong, J. C. Kang, H. Zhang, X. Sun, L. P. Zhang, Dr. J. Lin, Dr. Q. Luo, Prof. C.-Q. Ma
Suzhou Institute of Nano-Tech and Nano-Bionics
Chinese Academy of Sciences (CAS)
Suzhou 215123, P. R. China

Z. G. Wang, C. Gong, Dr. J. Lin, Prof. C.-Q. Ma
Suzhou Institute of Nano-Tech and Nano-Bionics Nanchang
Chinese Academy of Sciences (CAS)
Nanchang 330200, P. R. China

The ORCID identification number(s) for the author(s) of this article can be found under https://doi.org/10.1002/adfm.202007276.

DOI: 10.1002/adfm.202007276

this method is extremely suitable for large-area printing. Although there are several advantages associated with gravure printing, a few papers have described the preparation of AgNW electrodes,[38–40] and no studies have explored the use of gravure-printed silver nanowire electrodes in PSCs.

In this study, we demonstrate that large-area silver-nanowire-based transparent electrodes can be prepared using a gravure printing method. Through careful ink formulation and printing processing optimization, transparent AgNW electrodes with a sheet resistance of 10–30 Ω sq^{-1} and a high light transparency of 88–91% can be achieved. A smooth surface and excellent uniformity were also observed for the printed AgNW electrodes, rendering them excellent candidates for PSCs. Through device optimization, a high PCE of 13.61% and a high efficiency of 12.88% for a 1 cm^2 flexible AgNW electrode were achieved, thereby proving that gravure printing could be an ideal method for the preparation of large-area flexible PSCs.

2. Results and Discussion

2.1. Rheology of Silver Nanowire Inks

Figure 1a shows a schematic diagram of the gravure printing process. Gravure printing is mainly divided into three steps.[41,42] First, the doctor blade fills the ink into the gravure cavities (for a microscopic image of gravure cavities, see Figure S1 in the Supporting Information) while removing the ink in the nonpatterned area. Subsequently, the ink is transferred from the cavities of the gravure roller to the substrate under a specific pressure with the help of the impression roller. Finally, the ink is leveled on the substrate driven by its surface tension; subsequently, the solvent in the ink volatilizes, solidifying the film. Therefore, the wettability of the ink on the substrate is an important factor affecting the uniformity of the wet ink solution and the consequently formed solid thin film. The wettability between the ink and substrate is determined by the surface tension of the ink and surface energy of the substrate. Because the polyethylene terephthalate (PET) substrate used in this experiment is identical to that described above, the surface tension of the ink determines the wetting behaviors of the inks on the substrate.

The AgNW inks used in the present work consisted of a solvent solution of isopropanol (IPA) and water. The surface tension of the AgNW inks was tuned by adjusting the blend ratio of IPA and water to improve their suitability for gravure printing. Figure 1b,c shows the surface tension and viscosity curves of AgNW inks with different solvent ratios and AgNW concentrations, respectively, and the corresponding results are listed in **Table 1**. As shown in Figure 1b and Table 1, as the content of IPA increased from 0% to 90% and the surface tension of the ink decreased from 71.51 to 24.84 mN m^{-1}. This is because the surface tension of IPA (21.7 mN m^{-1}) is lower than that of water (71.8 mN m^{-1}). Figure 1c shows that the surface tension of the AgNW ink remained basically unchanged as the AgNW concentration increased. Therefore, the surface tension of the AgNW ink was primarily affected by the solvent ratio, while the AgNW concentration had a negligible effect.

Figure 1d,e shows the viscosity curves of AgNW inks with different solvent ratios and AgNW concentrations at different shear rates, and the corresponding performance parameters are shown in Figure 1b,c and listed in Table 1. All inks have been found to undergo shear thinning of the viscosity, suggesting that these inks are typical non-Newtonian fluids, which are beneficial for gravure printing.[42] Different shear rates were observed during the gravure printing process, which greatly influenced process efficiency. In the first ink filling step, the high shear rate between the doctor blade and the gravure roller thinned the ink, improving its ability to flow into the gravure cavities. In the process of ink transfer from the cavities to the substrate, the AgNW ink in the cavities was subjected to the shearing force between the gravure roller and the substrate (originally from the impression roller), and the shear thinning of the viscosity was conducive to the improved transfer of ink to the substrate. After the ink was transferred, the shearing force on the ink disappeared, and the increased viscosity of the AgNW ink prevented spreading. Therefore, the self-leveling characteristics of the inks determined the morphology of the final thin film. The blue curves in Figure 1b,c indicate the viscosity of AgNW inks with different solvent ratios and different AgNW concentrations at a shear rate of 1 s^{-1}. Figure 1b shows that the viscosity of the AgNW ink gradually increased as the content of IPA increased. This occurred because the viscosity of IPA (2.43 mPa s) is greater than that of water (1 mPa s). When the content of IPA reached 90%, the viscosity of the AgNW ink decreased significantly, which was ascribed to the poor dispersibility of AgNWs in a high content of IPA. Although the surface tension of AgNW inks did not change significantly as the AgNW concentration increased, the viscosity of the AgNW inks increased dramatically from 193.5 mPa s, yielding a 2 mg mL^{-1} dispersion to 1399.0 mPa s for 9 mg mL^{-1} ink. Such a viscosity increase may be ascribed to the more intensive interaction between AgNWs. These results demonstrated that both the surface tension and viscosity of the AgNW inks can be tuned by altering the solvent mixture and concentration variation, which facilitated the printing process.

2.2. Characteristics of Gravure-Printed Silver Nanowire Electrodes

Figure 2a–f shows the laser scanning microscopic (LSM) images of the gravure-printed AgNW electrodes from AgNW inks with different solvent mixture ratios. This figure illustrates that an uneven ribbing morphology of the printed AgNW networks was formed when the IPA content was low (10%), indicating that the wettability or self-leveling of the AgNW inks on the substrate was not satisfied, which was supported by the large contact angle of 55°–75° for the solvent dispersion of AgNW on the PET (Figure 2, insets). Note that the PET used for the preparation of the AgNW electrode was hydrophilic. The relatively high contact angle suggests that the surface tension of the initial silver nanowire ink was too high. Therefore, isopropanol was used to decrease the surface tension of the ink. Similar ribbing structures are commonly found in gravure-printed films, which can be suppressed by tuning the rheological properties of the inks and the drying process of the printed wet films.[42–44] As the content of IPA increased, the contact angle of the corresponding mixed solvent on the PET decreased, and

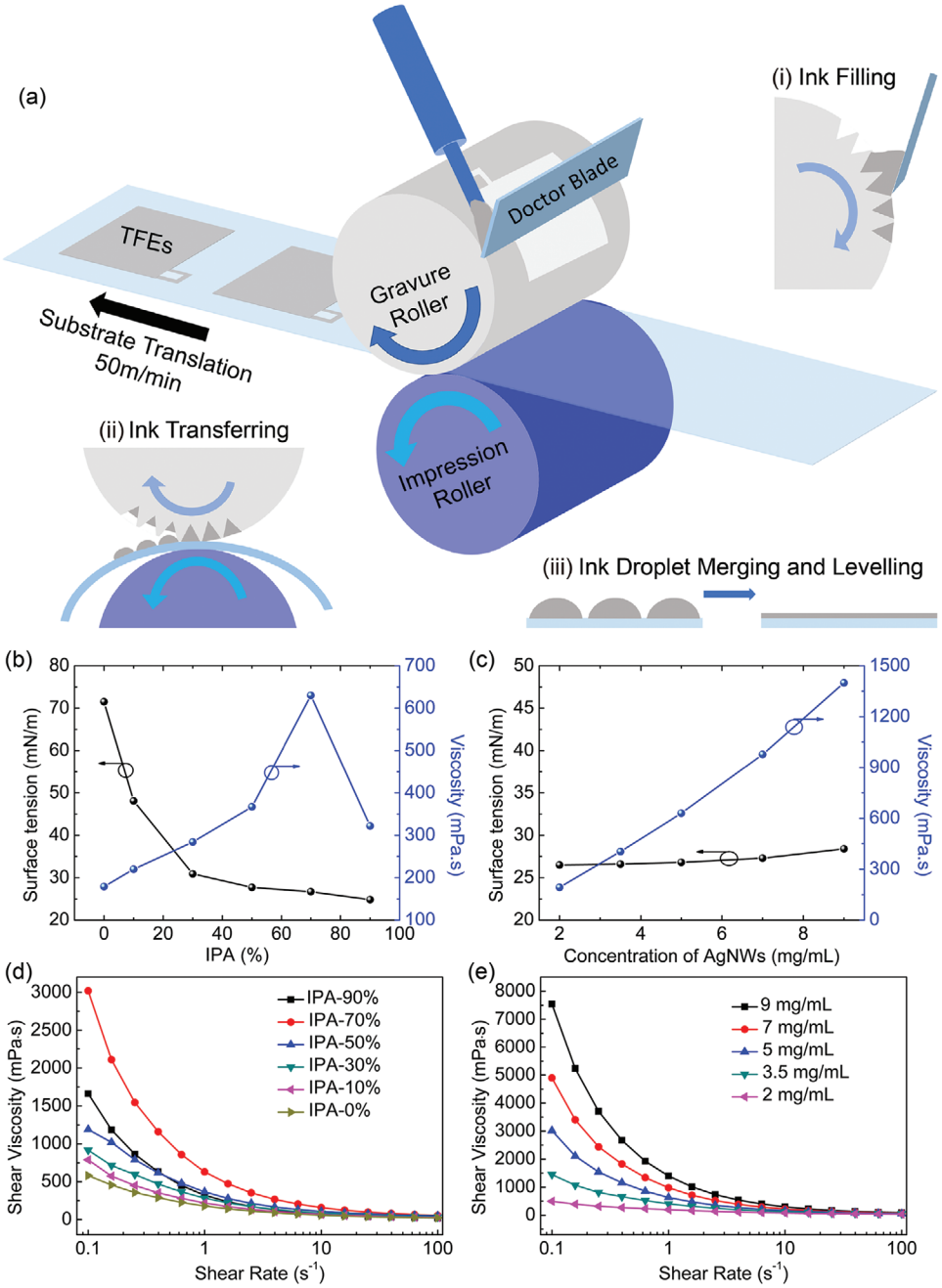

Figure 1. a) Schematic diagram of the high-speed gravure printing process used to print silver nanowire electrodes. Insets: i) the doctor blade forces the ink to fill the gravure cavities; ii) the ink is transferred from the cavities of the gravure roller to the substrate; and iii) ink leveling on the substrate. Surface tension and viscosity at a shear rate 1 s^{-1} from AgNW inks with b) different volume fractions of isopropanol and c) different AgNW concentrations. Viscosity of the formulations as a function of shear rate for d) different volume fractions of isopropanol and e) different AgNW concentrations.

the ribbing structure gradually weakened. When the content of IPA reached 50–70%, the ribbing structure disappeared. Since the higher viscosity of AgNW ink slows the self-leveling of the AgNW ink droplet, the high viscosity of the higher IPA content AgNW ink should not facilitate the elimination of the ribbing structure. Therefore, we attributed the improved film-forming ability of AgNW ink with higher IPA content to the lower surface tension of the AgNW ink, which improved wettability between the AgNW ink and the substrate surface. A further increase in IPA content to 90% led to the formation of a ribbing structure. This was attributed to the high IPA evaporation rate of the mixed solvent, which led to the rapid precipitation of silver nanowires and worsened the leveling of the AgNW ink droplets on the substrate.

The LSM images of the gravure-printed AgNW electrodes from AgNW inks with different AgNW concentrations are shown in Figure 2e,g–i (see Figure S2 in the Supporting Information for the film printed from 2 mg mL^{-1} AgNW ink). This

Table 1. Properties of gravure-printed AgNW electrodes from AgNW inks with different solvent ratios and different AgNW concentrations.

Entry	Concentration of AgNWs [mg mL^{-1}]	IPA [%]	Surface tension [mN m^{-1}]	Viscosity [mPa s]	T_{550nm}[a)] [%]	R_s[b)] [Ω sq^{-1}]	FoM	Ribbing structure[c)]
1	5	0	71.5	179.1	99.3	982.3 ± 423.8	56	++++++
2		10	48.1	219.9	98.9	177.2 ± 67.1	189	++++
3		30	30.9	284.1	98.9	52.6 ± 2.5	672	+
4		50	27.7	367	99.0	48.2 ± 1.6	763	–
5		70	26.7	630.2	99.0	47.8 ± 1.3	785	–
6		90	24.8	321.9	98.5	78.5 ± 15.9	322	++
7	2	70	26.5	193.5	99.7	159.7 ± 11.4	737	–
8	3.5		26.6	403.9	99.3	70.3 ± 4.2	763	–
9	5		26.8	630.2	98.9	45.1 ± 1.7	770	–
10	7		27.3	977.4	98.6	34.0 ± 1.3	754	+
11	9		28.4	1399.0	97.8	26.8 ± 1.4	638	++

[a)]Transmittance at 550 nm, substrate excluded; [b)]The average values of sheet resistance were calculated from 20 points on an 11 × 25 cm^2 AgNW electrode; [c)]The more the number of +, the more obvious the ribbing structure, and – means no ribbing structure.

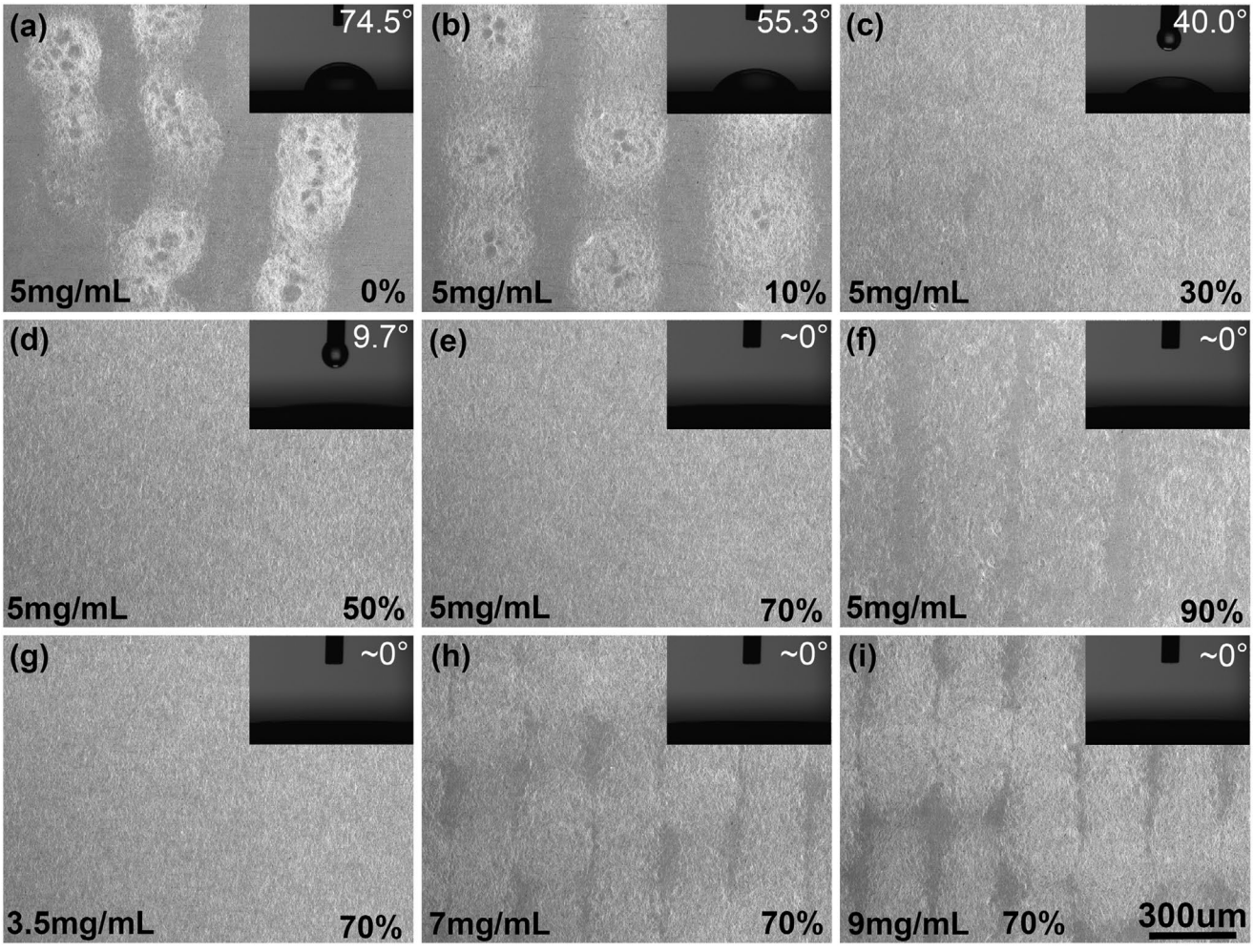

Figure 2. LSM images of the gravure-printed AgNW electrodes from AgNW inks with a–f) different volume fractions of isopropanol and g–i) different AgNW concentrations. Insets: the contact angle of the corresponding mixed solvent on the PET substrate.

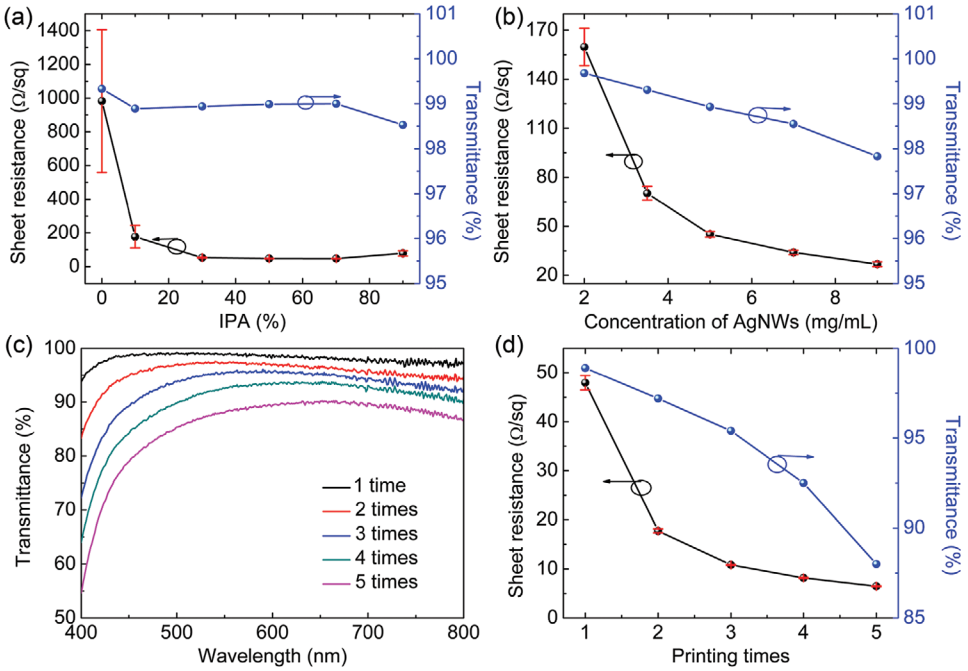

Figure 3. Sheet resistance and transmittance at 550 nm of the gravure-printed AgNW electrodes from AgNW inks with a) different volume fraction of isopropanol and b) different AgNW concentrations. The average values of sheet resistance were calculated from 20 points on an 11 × 25 cm^2 AgNW electrode. Error bars indicate the standard deviation. c) Transmission spectra of the gravure-printed AgNW electrodes based on different printing times. d) Sheet resistance and transmittance at 550 nm of the gravure-printed AgNW electrodes based on different printing times.

figure indicates that when the concentration of the AgNWs was lower than 5 mg mL^{-1} (Figure 2e, for 5 mg mL^{-1}), the obtained AgNW networks were homogeneous, and no ribbing structure was observed. However, when the AgNW concentration increased to 7 or 9 mg mL^{-1}, the ribbing structure appeared again for the printed AgNW electrodes. Since the surface tension of AgNW inks did not change significantly as the AgNW concentration increased (Figure 1c), the appearance of the ribbing structure was attributed to the high viscosity of the ink, which hindered the self-leveling of ink drops on the substrate.

Figure S3 (Supporting Information) shows the transmittance spectroscopy of the AgNW networks printed from different AgNW inks. The light transmittances of 550 nm and the measured sheet resistance of these printed AgNW films are summarized in Table 1. **Figure 3**a shows the correlation between the sheet resistance (R_s) and transmittance at 550 nm (T_{550nm}) of the printed AgNW electrodes to AgNW inks with different IPA contents. When the IPA content increased from 0% to 70%, the sheet resistance of the AgNW electrode was reduced from 982.3 ± 423.8 to 47.8 ± 1.3 Ω sq^{-1}, with greatly improved homogeneity. When the IPA content increased to 90%, the sheet resistance of the AgNW electrode increased to 78.5 ± 15.9 Ω sq^{-1}. This is in good accordance with the uniform morphology of AgNW networks (Figure 2a–f). In contrast, as the IPA content increased, the transmittance of the AgNW electrode was almost identical (Figure S3a, Supporting Information). The figure of merit (FoM) of the transparent electrode is defined by the ratio of direct current conductivity to the optical conductivity (σ_{dc}/σ_{op}) and is often used to evaluate the optoelectric performance of FTEs (see the "Experimental Section" for more information).[45] The FoM values of the printed AgNW electrodes are listed in Table 1. The AgNW electrode printed from AgNW ink with 70% IPA exhibited an FoM of 785, which is among the highest values for AgNW films.[29,36]

Figure 3b shows the correlation of R_s and T_{550nm} to AgNW ink concentrations. As AgNW concentrations increased, R_s and T_{550nm} gradually decreased (see Figure S3b in the Supporting Information for the transmittance spectra of these films), which can be understood by the fact that more silver nanowires were deposited onto the substrate as the AgNW concentration increased. Note that even at a high AgNW concentration of 9 mg mL^{-1}, the printed AgNW electrode showed an R_s of 26.8 ± 1.4 Ω sq^{-1} with a T_{550nm} of 97.8%. Because the ribbing structure was clearly observed for the AgNW electrodes with high AgNW-concentration inks, increasing the AgNW concentration further was not considered effective to further reduce the R_s.

We studied the effect of printing time on the performance of the AgNW electrodes. Figure 3c,d shows the transmission spectra and R_s, T_{550nm} of AgNW electrodes with different printing times, and the corresponding performance parameters are listed in **Table 2**. Figure 3d shows that the sheet resistance and transmittance of the AgNW electrodes gradually decreased as the number of printing times increased. The FoM value of the electrode printed twice was higher, reaching a value of 798. Not surprisingly, lower R_s and narrower R_s distributions were measured for the multiple printed AgNW films than those of the AgNW electrode printed from the AgNW ink with high concentration, which can be understood by a more homogeneous AgNW network prepared from a multiple printing process. Nevertheless, low R_s below 10 Ω sq^{-1} with excellent

Table 2. Photoelectric performance of the gravure-printed AgNW electrodes from AgNW inks (5 mg mL^{-1} in a mixture solvent of 70% IPA and 30% H_2O) with different printing times.

Printing times	T_{550nm}[a,b] [%]	R_s[a] [Ω sq^{-1}]	FoM [ave.]
1	98.9	48.0 ± 1.5	775 (711)
2	97.2	17.7 ± 0.4	798 (765)
3	95.4	10.8 ± 0.1	752 (730)
4	92.5	8.2 ± 0.1	593 (579)
5	88.0	6.5 ± 0.1	454 (442)

[a]Transmittance at 550 nm, substrate excluded; [b]The average values of sheet resistance were calculated from 20 points on an 11 × 25 cm^2 AgNW electrode.

homogeneity can be achieved, indicating that this type of electrode is applicable in PSCs.

2.3. Gravure Printing versus Spin Coating

Spin coating is a feasible method for preparing nano thin films that have been widely used in the lab. To better understand the difference in printed AgNW electrodes through different methods, we compared the conductivity and light transparency of the AgNW electrodes prepared by spin coating and gravure printing. We first optimized the concentration of AgNW inks and the spin-coating speed for the preparation of AgNW electrodes on a 2.5 cm × 2.5 cm PET substrate. Figure S4 (Supporting Information) shows the transmission spectra and R_s and T_{550nm} of AgNW electrodes to the concentrations of AgNW inks, and the corresponding performance parameters are listed in Table S1 (Supporting Information). As AgNW concentrations increased, R_s and T_{550nm} gradually decreased, which can be attributed to the deposition of more silver nanowires on the substrate with the increase in AgNW concentration. Figure S5 (Supporting Information) shows the transmission spectra, R_s, and T_{550nm} of AgNW electrodes with different spin speeds, and the corresponding performance parameters are listed in Table S2 (Supporting Information). Higher R_s and T_{550nm} were measured for the AgNW films prepared by a higher spin-coating speed, which can be understood by the fact that fewer silver nanowires were deposited onto the substrate as the spin speed increased. The highest FoM of 460 was obtained from 5 mg mL^{-1} AgNW ink at a spin speed of 2500 rpm, which is lower than that of the gravure-printed AgNW electrode (vide supra).

In our lab, the maximum size that we could spin-coat is 5.0 × 5.0 cm^2, whereas we could print a flexible AgNW electrode in a size of 11.0 × 25.0 cm^2 by gravure printing (**Figure 4**a). Figure 4b,c shows the statistical data of the sheet resistance and transmittance for the gravure-printed (PET/AgNWs-GV) and spin-coated AgNW electrodes (PET/AgNWs-SP), respectively. Figure 4b illustrates that the AgNW electrodes prepared by gravure printing showed an average R_s of 10.83 Ω sq^{-1} with a small standard deviation of 0.09, which is much better than that of spin-coated AgNW films (12.99 ± 0.94 Ω sq^{-1}). In addition, higher light transparency (95.40 ± 0.07%) was measured for the gravure-printed AgNW electrode than for the spin-coated films (93.65 ± 0.34%, Figure 4c), even when R_s was lower for the PET/AgNWs-GV films. Both results indicated that gravure printing could achieve much better uniformity for the final printed electrode, which was attributed to the fact that gravure printing uses microcavity arrays in the patterned area to accept the inks, and the transferred ink droplets must be homogeneously distributed over the substrate.

The transmission spectra of the PET/AgNWs-GV (with an R_s of 10.8 Ω sq^{-1}), PET/AgNWs-SP (with an R_s of 11.2 Ω sq^{-1}), and glass/ITO (with an R_s of 10.5 Ω sq^{-1}) electrodes are shown in Figure 4d. Except for the lower light transparency over 330–400 nm owing to the light absorption of silver nanowires, the transmittance of the PET/AgNWs-GV electrode is comparable to that of glass/ITO but significantly higher than that of the PET/AgNWs-SP electrode in the range of 400–1000 nm. The average transmittance values of the PET/AgNWs-GV, PET/AgNWs-SP, and glass/ITO electrodes were 85.78%, 82.22%, and 85.58% in the range of 500–1000 nm, respectively, suggesting that gravure-printed AgNW electrodes had better optical transparency than the spin-coated AgNW electrodes.

Based on the obtained light transparency and sheet resistance of the AgNW electrode prepared by different methods, the FoM values of the PET/AgNWs-GV and PET/AgNWs-SP electrodes were calculated, and the results are depicted in Figure 4e. The FoM values of the PET/AgNWs-GV electrodes were mainly distributed between 700 and 800 with a maximum value of 798 (Table 2), while the FoM values of the PET/AgNWs-SP electrodes are mainly distributed between 300 and 500 with a maximum value of 460 (Table S1, Supporting Information). The FoM value of the PET/AgNWs-GV electrode was higher than that of the PET/AgNWs-SP electrode, and the PET/AgNWs-GV electrode had better photoelectric performance.

To further understand the influence of the AgNW deposition method on the transparency and conductivity of the AgNW electrodes, the surface morphology of the AgNW films was investigated via scanning electron microscopy (SEM) and atomic force microscopy (AFM). The results are shown in **Figure 5** and Figure S6 (Supporting Information). For both films, the junction sites of AgNWs formed a close contact (Figure 5a,b), which helped reduce the contact resistance of the AgNWs and improved film conductivity.[46–48] However, the gravure-printed AgNWs were much more uniform (Figure 5c) than those of the spin-coated AgNW films (Figure 5d), where AgNW clusters could be clearly distinguished. Considering that no centrifugal force was applied to the ink droplets after the ink was transferred to the substrate during the gravure printing process, ink droplets dried much slower than in the spin-coating process in which a significant centrifugal force removed most of the silver ink solution, and only a small amount of ink remained. Therefore, the formation of AgNW clusters can be attributed to the rapid deposition of silver nanowires owing to the fast drying of ink solvents during spin coating. Figure 5e,f shows AFM images of the PET/AgNWs-GV PET/AgNWs-SP electrodes. The PET/AgNWs-GV electrodes (RMS = 11.1 nm) had a lower roughness than the PET/AgNWs-SP electrodes (RMS = 14.2 nm), which is in good accordance with the SEM results. Note that the surface roughness of the gravure-printed AgNW was much lower than that of metal grid electrodes,[16,49,50] making this type of electrode highly compatible for the preparation of high-performance OSCs.[17,51]

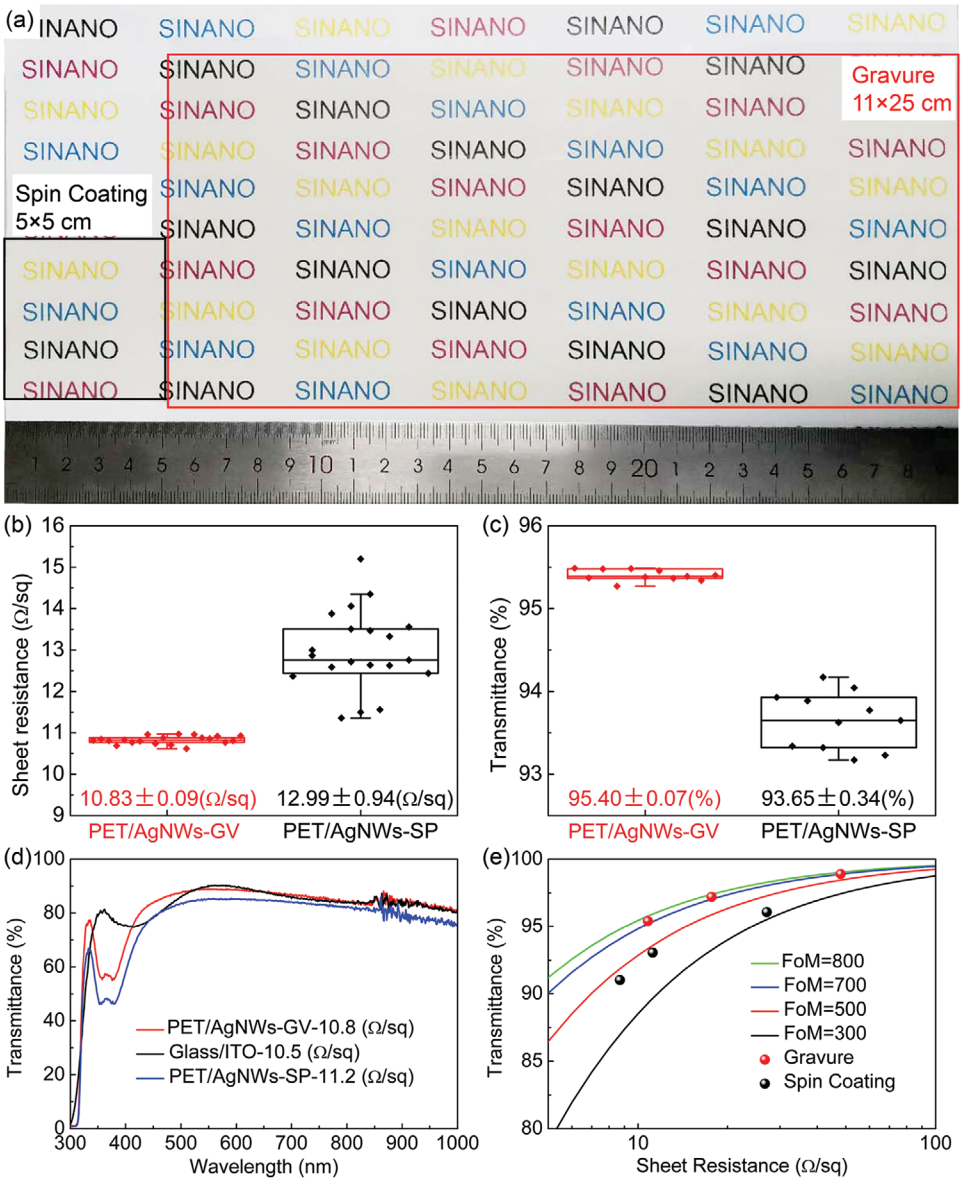

Figure 4. a) Photographs of the PET/AgNWs-GV (11 cm × 25 cm) and PET/AgNWs-SP (5 cm × 5 cm) electrodes. b) R_s and c) T_{550nm} of the PET/AgNWs-GV and PET/AgNWs-SP electrodes. The average values of R_s and T_{550nm} were, respectively, calculated from 20 points and 10 points on the PET/AgNWs-GV (11 cm × 25 cm) and PET/AgNWs-SP (5 cm × 5 cm) electrodes. d) Transmittance spectra of the PET/AgNWs-GV, PET/AgNWs-SP, and glass/ITO electrodes. e) Transmittance (at 550 nm) plotted as a function of film sheet resistance. The calculated FoM values for different electrodes are also shown in this figure.

2.4. Using Gravure-Printed AgNW Electrodes in PSCs

Figure 6a shows the device structure of the flexible OSCs based on the PET/AgNW electrode, and the molecular structure of the electron donor PM6 and electron acceptor Y6 for fabricating solar cells. Figure 6b shows the current density–voltage (J–V) curves of the devices based on PET/AgNWs-GV, PET/AgNWs-SP, and glass/ITO electrodes. The corresponding performance parameters are listed in **Table 3**. Regardless of whether the area of the device was 0.04 or 1 cm^2, the PCE of the PET/AgNWs-GV electrode-based solar cells was significantly higher than that of the device using the PET/AgNWs-SP electrode. Notably, the PCE of the 1 cm^2 flexible device prepared with the PET/AgNWs-GV electrode reached 13.61%, with an open-circuit voltage (V_{OC}) of 0.825 V, short-circuit current (J_{SC}) of 24.98 mA cm^{-2}, and a fill factor (FF) of 66.03%. To the best of our knowledge, a 13.61% PCE is the highest reported value to date for the 1 cm^2 flexible OSCs.[16,36] In contrast, the PCE of the 1 cm^2 device prepared by the PET/AgNWs-SP electrode was only 12.27%. The J_{SC} and FF of the devices were significantly lower than those of the PET/AgNWs-GV-based cells. It worth noting that although some of the AgNW-SP-based cells showed slightly higher PCE than that of the AgNW-GV cells, the averaged PCE of the AgNW-SP cells is lower than that of AgNW-GV cells and it is very difficult to

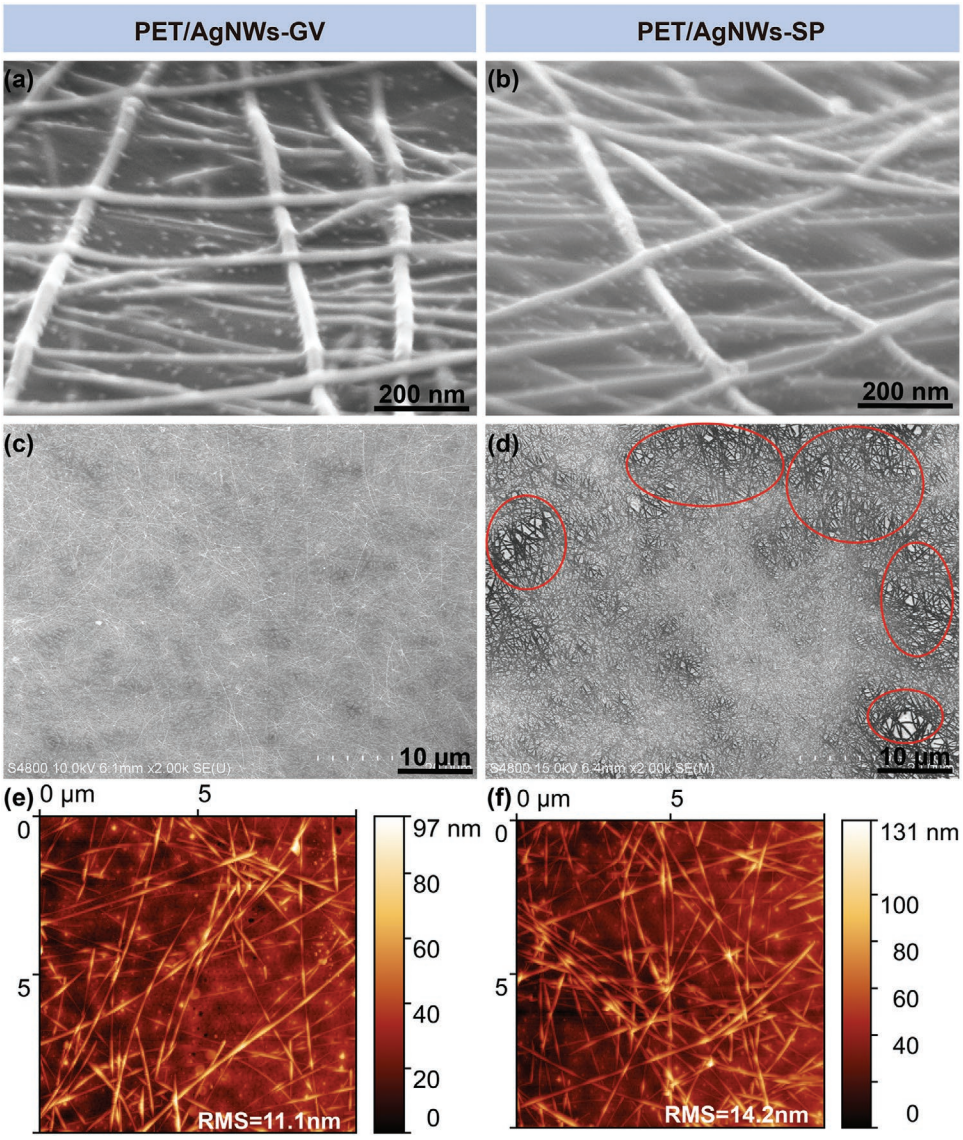

Figure 5. a–d) SEM images of a,c) the PET/AgNWs-GV and b,d) the PET/AgNWs-SP electrodes. e,f) AFM images of e) the PET/AgNWs-GV and f) the PET/AgNWs-SP electrodes.

further increase the device performance owing to the inhomogeneous AgNW surface. The 1 cm^2 flexible cell PCE was then checked at the National PV Industry Measurement and Testing Center of Fujian Metrology Institute, yielding a certified efficiency of 12.88% (see the Supporting Information for more details). The slightly lower device performance might be due to the air corrosion effect during post because the cells were sent without encapsulation. Nevertheless, the PCE reported here is the highest value for flexible PSCs with a cell area of 1 cm^2. For 0.04 cm^2 devices, the PCE of the device prepared by the PET/AgNWs-GV electrode was also significantly higher than that of the PET/AgNWs-SP electrode and is comparable to that of glass/ITO. Figure 6c shows the external quantum efficiency (EQE) spectra of these devices. The integrated currents calculated over the EQE spectra are in good agreement with the *J–V* curves. Figure 6d shows that the PCE of the device prepared by the PET/AgNWs-GV electrode was more concentrated than that of the PET/AgNWs-SP electrode, indicating that the device prepared by the PET/AgNWs-GV electrode has better repeatability. The PCE of the 1 cm^2 device was slightly lower than that of the corresponding small-area device, which may be mainly attributed to the decrease in FF. There are two possible explanations for this phenomenon. One is that the insufficient conductivity of the printed AgNW caused energy loss due to the high resistance of the electrode.[16] The other is the difficulty in achieving high uniformity for nano thin films during solar cell preparation.[10]

To further improve the PCE of the device, we studied the influence of the sheet resistance of the PET/AgNWs-GV electrode on device performance. Electrodes with sheet resistance values of 48.0, 17.7, and 10.8 Ω sq^{-1} were prepared through gravure printing Ag nanowires one, two, and three times on the PET substrates, respectively. The corresponding transmission spectra of these electrodes are shown in Figure 6e. Figure 6f

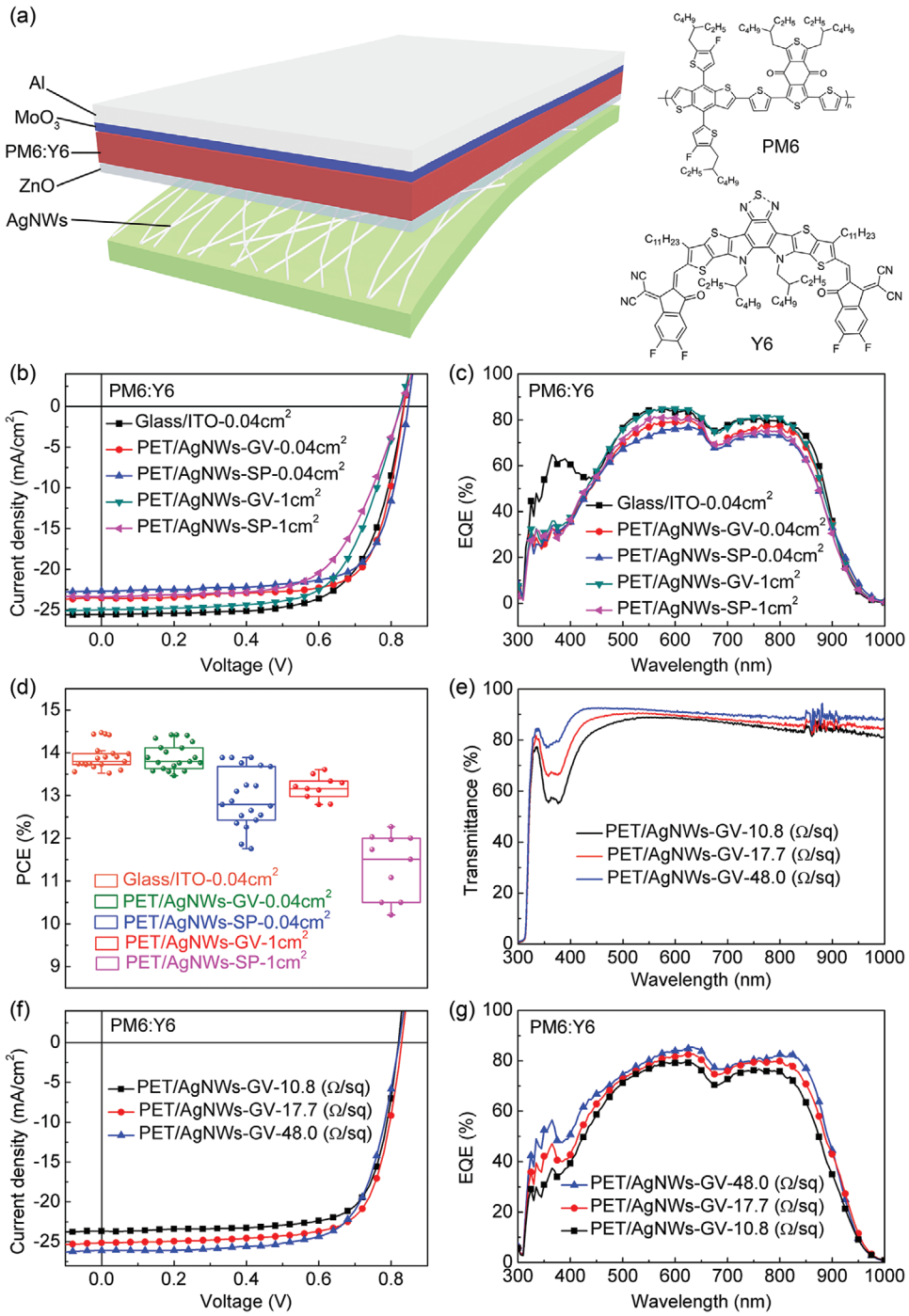

Figure 6. a) Device structure of the flexible OSCs and the molecular structure of the donor PM6 and the acceptor Y6. b) *J–V* curves and c) EQE spectra of the devices based on PET/AgNWs-GV, PET/AgNWs-SP, and glass/ITO electrodes. d) PCE distribution diagram of the devices based on PET/AgNWs-GV, PET/AgNWs-SP, and glass/ITO electrodes. e) Transmittance spectra of PET/AgNWs-GV electrodes with different sheet resistance. f) *J–V* curves and g) EQE spectra of the devices based on PET/AgNWs-GV electrodes with different sheet resistance values.

shows the *J–V* curves of the 0.04 cm^2 devices based on PET/AgNWs-GV electrodes with different sheet resistance values, and the corresponding performance parameters are listed in **Table 4**. Among the three devices, the one using the 17.7 Ω sq^{-1} AgNWs exhibited the highest performance of 15.28%, with a V_{OC} of 0.826 V, a J_{SC} of 25.14 mA cm^{-2}, and an FF of 73.60%. Increasing the sheet resistance of the electrode to 48.0 Ω sq^{-1} led to an improvement in J_{SC} from 25.14 to 26.12 mA cm^{-2}; however, FF dramatically decreased to 70.90%. In contrast, the decrease in sheet resistance caused an increase in FF and a decrease in J_{SC}. Figure 6g shows the EQE spectra of these devices. The integrated currents calculated over the EQE spectra

Table 3. Device performance of the PM6:Y6 solar cells with different electrodes.

Electrode	Sheet resistance [Ω sq^{-1}]	Area [cm^2]	V_{OC} [V]	J_{SC} [mA cm^{-2}]	FF [%]	PCE[a)] [%]
Glass/ITO	10.5	0.04	0.836	25.53	67.80	14.47 (13.92 ± 0.30)
PET/AgNWs-SP	11.2	0.04	0.845	22.66	72.54	13.89 (12.96 ± 0.66)
		1	0.828	23.38	63.42	12.27 (11.38 ± 0.71)
PET/AgNWs-GV	10.8	0.04	0.837	23.54	73.20	14.42 (13.92 ± 0.31)
		1	0.825	24.98	66.03	13.61 (13.18 ± 0.26)
PET/AgNWs-GV (certification)	10.8	1	0.8403	21.83	70.02	12.88

[a)]The average performance parameters of 1 and 0.04 cm^2 cells were calculated from 10 and 20 individual devices, respectively.

were in good agreement with the *J–V* curves. The variation in J_{SC} and FF was related to sheet resistance and optical transmission. A lower sheet resistance of the PET/AgNWs-GV electrode would benefit carrier collection and consequently increase the FF.[37] However, as the sheet resistance of the AgNW electrode decreases, the transmittance of the electrode also gradually decreases, resulting in a decrease in the J_{SC} of the device.[20,36] Therefore, it is necessary to carefully balance the sheet resistance and transmission of the electrode to achieve high device performance.

3. Conclusion

In summary, we demonstrated that silver-nanowire-based transparent electrodes can be prepared using a gravure printing method, which exhibits high potential for prepatterning and mass production. By changing the blend ratio of the mixed solvent and concentration of the AgNWs, the surface tension, viscosity, and volatilization rate of the AgNW inks can be tuned to meet the needs of gravure printing. With that, a large-area uniform-printed AgNW film was obtained with high conductivity ($R_s \approx$ 5–30 Ω sq^{-1}) and light transparency (82–91%). The highest FoM of the printed AgNW electrode approached 800 (with a sheet resistance of 17.7 Ω sq^{-1} and a high transparency of 97.2% at 550 nm). More importantly, owing to the homogeneous distribution of the AgNW ink droplets after being transferred to the substrate, a smooth surface and excellent uniformity were also achieved for the printed AgNW electrode, making them excellent candidates for PSCs. Through device optimization, high PCEs of 15.28% and 13.61% (certified efficiency of 12.88%) for small-area (0.04 cm^2) and large-area (1 cm^2) single-junction flexible PSCs were achieved, confirming that gravure printing could be an ideal method for the preparation of large-area flexible PSCs.

Table 4. Device performance of the PM6:Y6 solar cells based on PET/AgNWs-GV electrodes with different sheet resistance.

Sheet resistance [Ω sq^{-1}]	V_{OC} [V]	J_{SC} [mA cm^{-2}]	FF [%]	PCE[a)] [%]
48.0	0.821	26.12	70.90	15.21 (14.36 ± 0.56)
17.7	0.826	25.14	73.60	15.28 (14.75 ± 0.35)
10.8	0.820	23.68	74.08	14.38 (13.90 ± 0.27)

[a)]The average performance parameters were calculated from 20 individual devices.

4. Experimental Section

Materials: PM6 and Y6 were purchased from Solarmer Materials Inc. AgNW inks (10 mg mL^{-1} in H_2O or IPA with an average diameter of ≈25 nm and a length of ≈25 µm) were purchased from Nanchang Hechuang Advanced Materials (Nanchang, China). ZnO nanoparticles were synthesized as described by Beek et al.[52] 1-chloronaphthalene (CN, 97%) was purchased from TCI. Surface hydrophilic PET was purchased from Toyobo (Osaka, Japan).

Electrode Fabrication: By diluting and mixing the water-dispersed and isopropanol-dispersed AgNW inks (10 mg mL^{-1}, Nanchang H&C Advanced Materials Co., Ltd.), AgNW inks with different solvent ratios and concentrations can be obtained. To obtain the PET/AgNWs-GV electrodes, different formulations were printed on PET substrates using a gravure printing proof (D&R Lab Gravure Printer G-1100S, Suzhou D&R Instrum Co., Ltd.) at a speed of 50 m min^{-1}. The cavity volume per an area of the gravure roller was 13 mL m^{-2} with 50 lines cm^{-1}. The AgNW inks were spin-coated on PET at various spin speeds for 60 s to obtain the PET/AgNWs-SP electrodes. The FTEs were annealed at 120 °C for 10 min in an oven.

OSC Fabrication: Flexible OSCs with an inverted PET/AgNWs/ZnO/PM6:Y6/MoO_3/Al were fabricated on the PET/AgNW electrode. ZnO nanoparticles were spin-coated on top of the PET/AgNW at 800 rpm for 60 s and annealed at 120 °C for 10 min in a N_2-filled glove box. PM6:Y6 (D:A = 1:1.2, 16 mg mL^{-1} in total) was dissolved in chloroform (CF) with the solvent additive of CN (0.5%, v/v). Subsequently, the PM6:Y6 was spin-coated at 3000 rpm for 30 s on the ZnO layer and thermally annealed at 100 °C for 10 min. Finally, a MoO_3 layer (10 nm) and an Al layer (200 nm) were deposited on the active layer by vacuum evaporation at 6×10^{-4} Pa.

Characterization: The surface tension of AgNW inks was measured at 25 °C using a Kibron EZ-Pi^{plus} Surface Tensiometer (Finland). The viscosity of AgNW inks was measured at 25 °C using a Malvern Kinexus rheometer (Malvern, UK). The surface morphologies of the AgNW electrodes were characterized using a color 3D laser scanning microscope (VK-9710, KEYENCE, Osaka, Japan). The SEM images of the AgNW electrodes were measured using a Hitachi S4800 (Tokyo, Japan). The transmittance of the AgNW electrodes was measured using a Lamada 750 UV–vis–NIR spectrophotometer (PerkinElmer, Waltham, USA.). The roughness of the AgNW films was measured using AFM (Veeco Dimension 3100, New York, USA) in tapping mode. The sheet resistance of the AgNW electrodes was measured using a ST-2258C four-probe instrument (Suzhou Jingge Electronic, Suzhou, China).

The optoelectric performance of the FTEs was evaluated by the FoM, defined as σ_{dc}/σ_{op} in Equation (1)[45]

$$T(\lambda) = \left(1 + \frac{188.5\sigma_{op}(\lambda)}{R_S\sigma_{dc}}\right)^{-2} \quad (1)$$

where σ_{op} (λ), σ_{dc}, T (λ), and R_S, respectively, represent the optical conductivity (λ = 550 nm), the direct-current conductivity, the transmittance (λ = 550 nm), and the sheet resistance of the film, respectively.

The *J–V* measurements were performed in a nitrogen glove box with a Keithley 2400 source meter under simulated AM 1.5G solar illumination (100 mW cm^{-2}) generated by a Zolix SS150 solar simulator. EQE values were measured under simulated 1 sun operation conditions using bias light from a 532 nm solid state laser (Changchun New Industries, MGL-III-532).

Supporting Information

Supporting Information is available from the Wiley Online Library or from the author.

Acknowledgements

This work was supported by the National Natural Science Foundation of China (Grant No. 51773224), Youth Innovation Promotion Association (Grant No. 2019317), and International Joint Project (Project No. GJHZ2092-019) of Chinese Academy of Sciences, and Suzhou Institute of Nano-Tech and Nano-Bionics Nanchang (Project Nos. 2017CA01 and 2019DH17).

Conflict of Interest

The authors declare no conflict of interest.

Keywords

gravure printing, large-area flexible electrodes, polymer solar cells, silver nanowires, surface morphology

Received: August 26, 2020
Revised: September 26, 2020
Published online:

[1] R. Sun, Q. Wu, J. Guo, T. Wang, Y. Wu, B. Qiu, Z. Luo, W. Yang, Z. Hu, J. Guo, M. Shi, C. Yang, F. Huang, Y. Li, J. Min, *Joule* **2020**, *4*, 407.
[2] L. Sun, W. Zeng, C. Xie, L. Hu, X. Dong, F. Qin, W. Wang, T. Liu, X. Jiang, Y. Jiang, Y. Zhou, *Adv. Mater.* **2020**, *32*, 1907840.
[3] T. Y. Qu, L. J. Zuo, J. D. Chen, X. Shi, T. Zhang, L. Li, K. C. Shen, H. Ren, S. Wang, F. M. Xie, Y. Q. Li, A. K. Y. Jen, J. X. Tang, *Adv. Opt. Mater.* **2020**, *8*, 2000669.
[4] Y. Cui, H. Yao, J. Zhang, T. Zhang, Y. Wang, L. Hong, K. Xian, B. Xu, S. Zhang, J. Peng, Z. Wei, F. Gao, J. Hou, *Nat. Commun.* **2019**, *10*, 2515.
[5] J. Gao, W. Gao, X. Ma, Z. Hu, C. Xu, X. Wang, Q. An, C. Yang, X. Zhang, F. Zhang, *Energy Environ. Sci.* **2020**, *13*, 958.
[6] K. Jiang, Q. Wei, J. Y. L. Lai, Z. Peng, H. K. Kim, J. Yuan, L. Ye, H. Ade, Y. Zou, H. Yan, *Joule* **2019**, *3*, 3020.
[7] J. Yuan, Y. Zhang, L. Zhou, G. Zhang, H.-L. Yip, T.-K. Lau, X. Lu, C. Zhu, H. Peng, P. A. Johnson, M. Leclerc, Y. Cao, J. Ulanski, Y. Li, Y. Zou, *Joule* **2019**, *3*, 1140.
[8] Y. Cui, H. Yao, J. Zhang, K. Xian, T. Zhang, L. Hong, Y. Wang, Y. Xu, K. Ma, C. An, C. He, Z. Wei, F. Gao, J. Hou, *Adv. Mater.* **2020**, *32*, 1908205.
[9] L. Zhu, M. Zhang, G. Zhou, T. Hao, J. Xu, J. Wang, C. Qiu, N. Prine, J. Ali, W. Feng, X. Gu, Z. Ma, Z. Tang, H. Zhu, L. Ying, Y. Zhang, F. Liu, *Adv. Energy Mater.* **2020**, *10*, 1904234.
[10] B. Fan, Z. Zeng, W. Zhong, L. Ying, D. Zhang, M. Li, F. Peng, N. Li, F. Huang, Y. Cao, *ACS Energy Lett.* **2019**, *4*, 2466.
[11] K. Li, Y. Wu, Y. Tang, M. A. Pan, W. Ma, H. Fu, C. Zhan, J. Yao, *Adv. Energy Mater.* **2019**, *9*, 1901728.
[12] Q. Liao, Q. Kang, Y. Yang, C. An, B. Xu, J. Hou, *Adv. Mater.* **2020**, *32*, 1906557.
[13] G. Ji, W. Zhao, J. Wei, L. Yan, Y. Han, Q. Luo, S. Yang, J. Hou, C.-Q. Ma, *J. Mater. Chem. A* **2019**, *7*, 212.
[14] R. Yu, H. Yao, Y. Cui, L. Hong, C. He, J. Hou, *Adv. Mater.* **2019**, *31*, 1902302.
[15] Q. Liu, Y. Jiang, K. Jin, J. Qin, J. Xu, W. Li, J. Xiong, J. Liu, Z. Xiao, K. Sun, S. Yang, X. Zhang, L. Ding, *Sci. Bull.* **2020**, *65*, 272.
[16] Y. Han, X. Chen, J. Wei, G. Ji, C. Wang, W. Zhao, J. Lai, W. Zha, Z. Li, L. Yan, H. Gu, Q. Luo, Q. Chen, L. Chen, J. Hou, W. Su, C. Q. Ma, *Adv. Sci.* **2019**, *6*, 1901490.
[17] W. Li, H. Zhang, S. Shi, J. Xu, X. Qin, Q. He, K. Yang, W. Dai, G. Liu, Q. Zhou, H. Yu, S. R. P. Silva, M. Fahlman, *J. Mater. Chem. C* **2020**, *8*, 4636.
[18] Y. Zhang, S.-W. Ng, X. Lu, Z. Zheng, *Chem. Rev.* **2020**, *120*, 2049.
[19] Y. Li, G. Xu, C. Cui, Y. Li, *Adv. Energy Mater.* **2018**, *8*, 1701791.
[20] D. Koo, S. Jung, J. Seo, G. Jeong, Y. Choi, J. Lee, S. M. Lee, Y. Cho, M. Jeong, J. Lee, J. Oh, C. Yang, H. Park, *Joule* **2020**, *4*, 1021.
[21] W. Zhang, W. Song, J. Huang, L. Huang, T. Yan, J. Ge, R. Peng, Z. Ge, *J. Mater. Chem. A* **2019**, *7*, 22021.
[22] H.-Q. Cui, R.-X. Peng, W. Song, J.-F. Zhang, J.-M. Huang, L.-Q. Zhu, Z.-Y. Ge, *Chin. J. Polym. Sci.* **2019**, *37*, 760.
[23] T. Yan, W. Song, J. Huang, R. Peng, L. Huang, Z. Ge, *Adv. Mater.* **2019**, *31*, 1902210.
[24] J. Wang, X. Chen, F. Jiang, Q. Luo, L. Zhang, M. Tan, M. Xie, Y.-Q. Li, Y. Zhou, W. Su, Y. Li, C.-Q. Ma, *Sol. RRL* **2018**, *2*, 1800118.
[25] G. Zeng, J. Zhang, X. Chen, H. Gu, Y. Li, Y. Li, *Sci. China: Chem.* **2019**, *62*, 851.
[26] K. W. Seo, J. Lee, J. Jo, C. Cho, J. Y. Lee, *Adv. Mater.* **2019**, *31*, 1902447.
[27] R. Peng, Z. Wan, W. Song, T. Yan, Q. Qiao, S. Yang, Z. Ge, M. Wang, *ACS Appl. Mater. Interfaces* **2019**, *11*, 42447.
[28] J. H. Seo, I. Hwang, H. D. Um, S. Lee, K. Lee, J. Park, H. Shin, T. H. Kwon, S. J. Kang, K. Seo, *Adv. Mater.* **2017**, *29*, 1701479.
[29] Y. Sun, M. Chang, L. Meng, X. Wan, H. Gao, Y. Zhang, K. Zhao, Z. Sun, C. Li, S. Liu, H. Wang, J. Liang, Y. Chen, *Nat. Electron.* **2019**, *2*, 513.
[30] J. Kang, K. Han, X. Sun, L. Zhang, R. Huang, I. Ismail, Z. Wang, C. Ding, W. Zha, F. Li, Q. Luo, Y. Li, J. Lin, C.-Q. Ma, *Org. Electron.* **2020**, *82*, 105714.
[31] X. Sun, W. Zha, T. Lin, J. Wei, I. Ismail, Z. Wang, J. Lin, Q. Luo, C. Ding, L. Zhang, Z. Su, B. Chu, D. Zhang, C.-Q. Ma, *J. Mater. Sci.* **2020**, *55*, 14893.
[32] K. Han, M. Xie, L. Zhang, L. Yan, J. Wei, G. Ji, Q. Luo, J. Lin, Y. Hao, C.-Q. Ma, *Sol. Energy Mater. Sol. Cells* **2018**, *185*, 399.
[33] M. Xie, H. Lu, L. Zhang, J. Wang, Q. Luo, J. Lin, L. Ba, H. Liu, W. Shen, L. Shi, C. Q. Ma, *Sol. RRL* **2018**, *2*, 1700184.
[34] F. Guo, N. Li, V. V. Radmilović, V. R. Radmilović, M. Turbiez, E. Spiecker, K. Forberich, C. J. Brabec, *Energy Environ. Sci.* **2015**, *8*, 1690.
[35] H. Tang, H. Feng, H. Wang, X. Wan, J. Liang, Y. Chen, *ACS Appl. Mater. Interfaces* **2019**, *11*, 25330.
[36] X. Chen, G. Xu, G. Zeng, H. Gu, H. Chen, H. Xu, H. Yao, Y. Li, J. Hou, Y. Li, *Adv. Mater.* **2020**, *32*, 1908478.
[37] J. Kim, D. Ouyang, H. Lu, F. Ye, Y. Guo, N. Zhao, W. C. H. Choy, *Adv. Energy Mater.* **2020**, *10*, 1903919.
[38] J. D. Park, S. Lim, H. Kim, *Thin Solid Films* **2015**, *586*, 70.
[39] W. J. Scheideler, J. Smith, I. Deckman, S. Chung, A. C. Arias, V. Subramanian, *J. Mater. Chem. C* **2016**, *4*, 3248.
[40] Y. Peng, B. Du, X. Xu, J. Yang, J. Lin, C. Ma, *Appl. Phys. Express* **2019**, *12*, 066503.

[41] R. Kitsomboonloha, S. J. Morris, X. Rong, V. Subramanian, *Langmuir* **2012**, *28*, 16711.
[42] G. Hernandez-Sosa, N. Bornemann, I. Ringle, M. Agari, E. Dörsam, N. Mechau, U. Lemmer, *Adv. Funct. Mater.* **2013**, *23*, 3164.
[43] J. J. Michels, S. H. P. M. de Winter, L. H. G. Symonds, *Org. Electron.* **2009**, *10*, 1495.
[44] A. de la Fuente Vornbrock, D. Sung, H. Kang, R. Kitsomboonloha, V. Subramanian, *Org. Electron.* **2010**, *11*, 2037.
[45] S. De, T. M. Higgins, P. E. Lyons, E. M. Doherty, P. N. Nirmalraj, W. J. Blau, J. J. Boland, J. N. Coleman, *ACS Nano* **2009**, *3*, 1767.
[46] Y. Liu, J. Zhang, H. Gao, Y. Wang, Q. Liu, S. Huang, C. F. Guo, Z. Ren, *Nano Lett.* **2017**, *17*, 1090.
[47] K. Zhang, J. Li, Y. Fang, B. Luo, Y. Zhang, Y. Li, J. Zhou, B. Hu, *Nanoscale* **2018**, *10*, 12981.
[48] H. Kang, S. J. Song, Y. E. Sul, B. S. An, Z. Yin, Y. Choi, L. Pu, C. W. Yang, Y. S. Kim, S. M. Cho, J. G. Kim, J. H. Cho, *ACS Nano* **2018**, *12*, 4894.
[49] Y. Li, L. Mao, Y. Gao, P. Zhang, C. Li, C. Ma, Y. Tu, Z. Cui, L. Chen, *Sol. Energy Mater. Sol. Cells* **2013**, *113*, 85.
[50] Y. Li, L. Meng, Y. M. Yang, G. Xu, Z. Hong, Q. Chen, J. You, G. Li, Y. Yang, Y. Li, *Nat. Commun.* **2016**, *7*, 10214.
[51] X. Y. Dong, P. Shi, L. L. Sun, J. Li, F. Qin, S. X. Xiong, T. F. Liu, X. S. Jiang, Y. H. Zhou, *J. Mater. Chem. A* **2019**, *7*, 1989.
[52] W. J. Beek, M. M. Wienk, M. Kemerink, X. Yang, R. A. Janssen, *J. Phys. Chem. B* **2005**, *109*, 9505.